Journal of Catalysis 260 (2008) 217–226

Contents lists available at ScienceDirect

Journal of Catalysis

www.elsevier.com/locate/jcat

Growth of filamentous carbon by decomposition of ethanol on nickel foam: Influence of synthesis conditions and catalytic nanoparticles on growth yield and mechanism

Namjo Jeong [a,b], Junghoon Lee [b,*]

[a] Nanomaterials Research Center, Korea Institute of Energy Research, Daejeon 305-343, Korea
[b] School of Mechanical and Aerospace Engineering, Institute of Advanced Machinery and Design, Seoul National University, Seoul 151-744, Korea

ARTICLE INFO

Article history:
Received 5 May 2008
Revised 23 September 2008
Accepted 7 October 2008
Available online 31 October 2008

Keywords:
Ethanol
Filamentous carbon
Nickel foam
Nickel carbide
Surface break-up

ABSTRACT

This paper presents nano-sized carbon filaments grown by catalytic decomposition of ethanol on polycrystalline nickel foam. Our study is focused on the effects of synthesis conditions on the formation of filamentous carbon. The formation rate of filamentous carbon increased as the supply of liquid ethanol into the furnace and the synthesis time increased during growth process, whereas H_2 concentration in carrier gas had the opposite effect. The most favorable temperature for the highest formation rate was around 600 °C. We investigated the role of catalytic nanoparticles in the growth mechanism of filamentous carbon. Tip growth was the primary mechanism responsible for growth of the filamentous carbon; octopus-like carbon filaments were formed on large nanoparticles of about 100 nm in diameter. It was also discovered that surface break-up on the nickel foam precipitated the formation of filamentous carbon. We detected the presence of Ni_3C as synthesis conditions after a long exposure to ethanol.

1. Introduction

Carbon nanotubes (CNTs) and carbon nanofibers (CNFs) are nano-sized filamentous carbon materials with an interlayer spacing similar to that of bulk graphite [1]. The filamentous carbon that can be formed during many metal-catalyzed reaction processes, including steam reforming and Fisher–Tropsch synthesis, often causes serious problems of catalysts deactivation and increased pressure drop in porous structures such as honeycomb and mesh. Nevertheless, carbon filaments are good candidates for various applications due to their excellent properties, such as high surface area, considerable aspect ratio, high mechanical strength, and high electrical conductivity [2,3]. Transition metals, such as nickel, iron, and cobalt, are the most commonly used catalysts for the growth of filamentous carbon [4–6]. These metals are most often used as thin-films or nano-sized particles on substrates such as glass or silicon wafer [7,8]. However, the traditional approaches, that use catalytic metals on substrates can lead to the loss of mechanical anchoring or insufficient electrical contact between the nanofilaments and the substrates due to poor adhesion of the metals. Direct growth of filamentous carbon on a metallic substrate, rather than on a heterogeneous substrate, enhances adhesion, thereby extending the applications of the carbon filaments [9,10].

Nickel is one of the most suitable catalytic metals for the direct growth on the metallic substrates. This metal has been extensively studied for the formation of filamentous carbon by catalytic decomposition of carbon source [11], and for the use as a substrate with high electroactivity by electrochemists [12]. To date, some studies have reported the growth of CNTs on various nickel substrates. Wunderlich demonstrated the direct growth of CNTs via the tip growth mechanism on a nickel sheet by plasma CVD [13]. Kukovitsky et al. showed the formation of CNT films on mechanically and chemically pre-treated nickel foil using a thermal CVD apparatus [14]. Carbon filaments with uniform shape, size, and structure can be easily synthesized on 2D plates, such as foil and sheet, because decomposition and deposition of the carbon source are uniform on the plate surfaces. In contrast, growth of filamentous carbon on 3D substrates, such as foam and mesh, is challenging. The formation of filamentous carbon on highly porous substrates is a complicated process that causes a non-uniform surface reaction between the carbon source and the surface of the substrate. A few methods that use nickel foam to synthesize filamentous carbons have been explored [15–17]. Jarrah et al. showed a catalytic formation of CNFs on nickel foam using ethene [15,16]. They explained in detail the effects of the morphology and surface properties on the growth of CNFs, and also suggested that the presence of NiO has a significant positive effect on the increase of CNF formation.

In this work, we report the first direct synthesis of filamentous carbon on nickel foam using ethanol. The focus of our work is

* Corresponding author. Fax: +82 2 880 9101.
E-mail address: jleenano@snu.ac.kr (J. Lee).

0021-9517/$ – see front matter
doi:10.1016/j.jcat.2008.10.006

to investigate the effects of the synthesis conditions, such as synthesis temperature, synthesis time, H_2 concentration in carrier gas, and the amount of liquid ethanol supplied into the furnace, on the formation of filamentous carbon on the nickel foam. In addition, we studied the role of catalytic nanoparticles in the growth of filamentous carbon. The growth mechanisms on the polycrystalline nickel foam using ethanol with and without surface break-up were explained.

2. Experiments

2.1. Materials

The nickel foam was obtained from Changsha Lyrun Materials Co., Ltd., China. According to ICP analysis using an ICP-OES 4300DV (Perkin–Elmer, Co., USA), the nickel foam had ~99.9% of Ni and others such as Fe, Si, Al, C in ppm order. Samples of nickel foam with dimensions of 10 mm × 10 mm × 1.5 mm ($W \times L \times t$) and weighing approximately 50 mg were prepared for the growth of filamentous carbon. Pore size was in a range of 100–200 μm. The number of pores per inch (PPI) was about 110 and porosity was above 95%. The nickel foam was placed perpendicular to the direction of the carrier gas flow for the effective growth of the filamentous carbon. Nitrogen (99.999%), hydrogen (99.999%, Safty-gas), and ethanol (99.5% dehydrated with maximum 0.005% water, Merck) were used for the formation of the filamentous carbon.

2.2. Catalytic growth of filamentous carbon

The carbon filaments were synthesized in a quartz tube reactor with dimensions of 32 mm × 400 mm × 2 mm ($d \times L \times t$). Prior to the growth process, the nickel foam substrate was reduced for 1 h at temperatures ranging between 550 and 750 °C in a H_2 atmosphere. The synthesis time was set up from 10 to 120 min. The synthesis temperature was raised to the desired range (550 and 750 °C) at a rate of 10 °C/min. Nitrogen gas at a flow rate of 100 ml/min was used as the main carrier gas with supplemental hydrogen at a rate of 0–100 ml/min. Liquid ethanol was used as a carbon source in our study of the growth of filamentous carbons on nickel foam. The ethanol was supplied at the rate of 2–5 cc/h to an ultrasonic atomizer with a vibrating plate and an on/off controller [18]. The ethanol was scattered as aerosols at the plate, introduced into the reactor, and then vaporized instantly upon exposure to the high temperature. When the carbon source was no longer supplied to the reactor the supply of hydrogen gas was terminated, and only nitrogen gas was introduced into the reactor at 100 ml/min. Then the furnace was cooled down to room temperature.

2.3. Characterization

After the formation of the filamentous carbon, weight of as-formed products was first measured to the fifth decimal place using a balance (Mettler AE 240) placed in a vacuum chamber. Carbon formation rate was calculated by measuring the weight of the nickel foam before and after synthesis. Then in order to minimize the effect of air on the decomposition of Ni_3C, the XRD measurement was immediately performed, and the scanning electron microscopy (SEM) and transmission electron microscope (TEM) images were obtained within 1–2 days.

For the characterization of surface morphology and structure, we collected the grown products from the reactor, and used various analysis techniques. The field emission SEM (FE-SEM) was performed (Hitachi S-4700) at an accelerating voltage of 10 kV. SEM-EDX (energy dispersive X-ray spectrometer) also was performed (Horiba 7200-H). To obtain the high resolution SEM images, surface of the sample was coated with an osmium coater (HPC-1SW) for 5 sec [19]. The peak corresponding to osmium component was barely observed in the EDX graph because of small amount of coating. Raman spectroscopy was performed using a LabRam HR with an Ar-ion laser 514 nm. The wave number was controlled between 100 and 3500 cm^{-1}. The radial breathing mode of single-walled carbon nanotubes was not observed. X-ray diffraction patterns of metallic nickel, Ni_3C, and the graphite structure were measured using a Rigaku Miniflex Instrument with Cu$K\alpha$ radiation at room temperature. TEM-JEM 2000FXII instrument and JEOL JEM 2010 were used for the TEM analysis. To obtain samples to be placed on a TEM grid made of carbon-coated Cu grid, the nickel foam with as-grown carbon filaments was soaked in a beaker of DI water, followed by ultrasonication for 10 min. A droplet of the solution was placed on the TEM grid, and dried at room temperature.

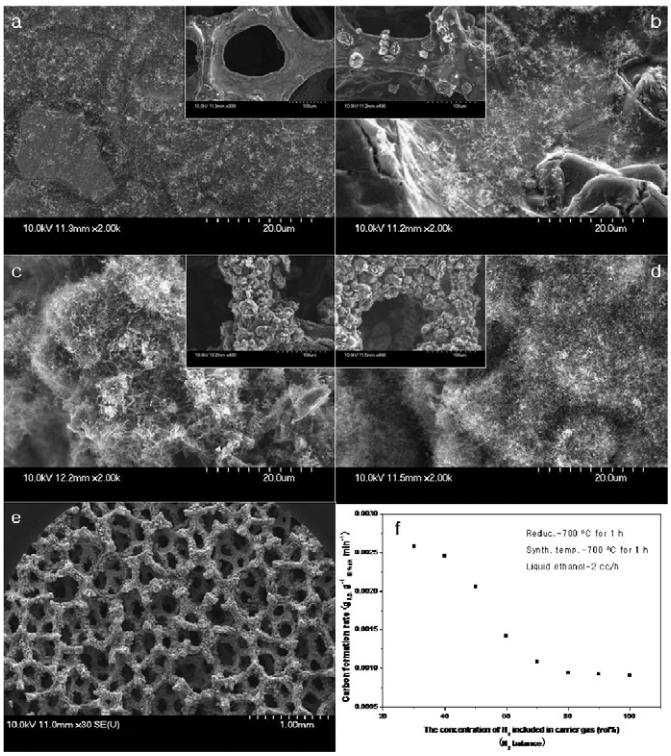

Fig. 1. SEM images of filamentous carbon formed on the nickel foam at 700 °C using different H_2 concentrations with respect to the carrier gas (liquid ethanol was supplied at a constant rate of 2 cc/h): (a) 100 vol% (i.e., no N_2), (b) 50, (c) 40, and (d) 30 vol% in N_2, (e) a low magnification image of (d); (f) shows the plot of the carbon formation rate versus H_2 concentrations in the carrier gas. The nickel foams were reduced at 700 °C for 1 h in 30 vol% H_2 in N_2.

3. Results and discussion

3.1. Effect of synthesis conditions on the formation rate of the filamentous carbons

Figs. 1a–1d shows the SEM images of filamentous carbon synthesized at 700 °C for 1 h with different H_2 concentrations in carrier gas during the growth. The prepared nickel foam was reduced at 700 °C for 1 h using 30 vol% H_2 in N_2 balance. Liquid ethanol was constantly supplied at a rate of 2 cc/min. As shown in Fig. 1a (100 vol% H_2 without N_2 in carrier gas), the growth yield of as-formed filamentous carbon was very low. The foam surface and the grain boundary did not show any damage. In Fig. 1b (50 vol% H_2 in N_2), the cracked shapes are found in some area of the foam surface (e.g., the inset). Some carbonaceous material

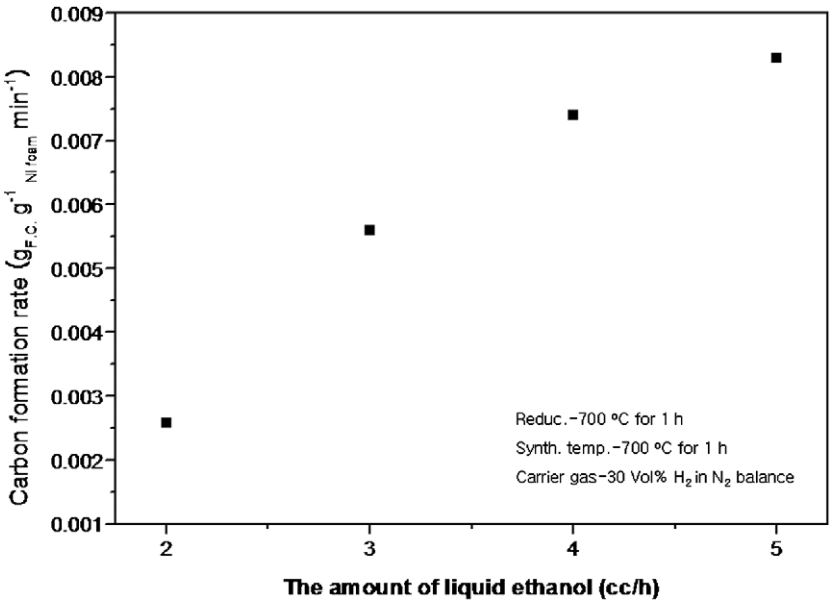

Fig. 2. Carbon formation rate vs the amount of liquid ethanol supplied into the furnace: the nickel foams were prepared by reducing in 30 vol% H_2 in N_2.

was formed at the damaged surface. However, carbon formation on the non-damaged surface predominated. Fig. 2c shows that the formation of filamentous carbon increased rapidly. As-grown filaments appeared irregular compared with those shown in Figs. 1a and 1b. Carbon formation gradually increased as H_2 concentrations in the carrier gas decreased to 30 vol% (Fig. 1d). Fig. 1e, which is a low magnification image of Fig. 1d, shows that the foam surface was completely covered with carbon. Fig. 1f shows plots of the carbon formation rate vs the H_2 concentrations in the carrier gas. These plots clearly reveal that the carbon formation rate on the nickel foam increased as the H_2 concentrations in the carrier gas decreased. This result implies that the lower H_2 concentration in the carrier gas leads to the better precipitation of carbon formation on the nickel foam, although it is not obvious whether the quality of as-formed carbon became better.

The role of H_2 in carbon deposition and/or formation over a metal catalytic surface has been reported. Jablonski et al. suggested that H_2 plays a key role in determination of the carbon morphology from the metal catalysts [20]. Baird et al. claimed that the high carbon deposition rate is related to the well-formed carbon morphologies [21]. Nishiyama and Tamai demonstrated that H_2 removes the surface carbon that hinders the catalytic action of the metal surface and the chemisorbed species that are precursors of deposition. They also concluded that the growth rate of the filamentous carbon increases as the H_2 concentration in the carrier gas increases [22]. As shown in Fig. 1, however, we found that the carbon formation rate on the nickel foam increased as the H_2 concentration in the carrier gas decreased. In this respect, our results do not seem consistent with the model proposed by Nishiyama and Tamai [22]. In their model, the surface break-up that can promote the carbon formation was not considered. Our surface break-up model on polycrystalline nickel foam will be further developed using additional results.

Fig. 2 shows the plots of the carbon formation rate vs the amount of liquid ethanol supplied into the furnace. Filamentous carbon was formed at 700 °C for 1 h with the supply of liquid ethanol at a rate of 2–5 cc/h. The nickel foam was reduced at 700 °C for 1 h, and 30 vol% H_2 in N_2 was used as the carrier gas during all processes. The carbon formation rate on the nickel foam increased as the amount of liquid ethanol increased.

Fig. 3a shows the plot of carbon formation rate vs synthesis time. The carbon filaments were formed at 700 °C when liquid

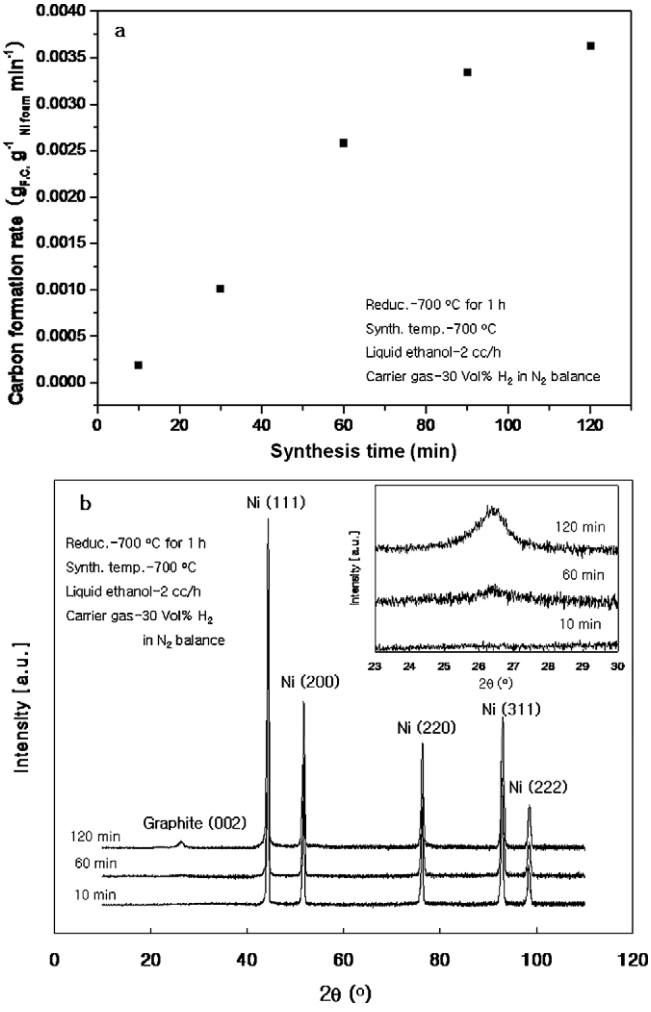

Fig. 3. (a) Carbon formation rate vs synthesis time when the liquid ethanol was supplied at a rate of 2 cc/min, (b) XRD patterns corresponding to (a). The nickel foams were reduced at 700 °C for 1 h in 30 vol% H_2 in N_2. The insert of (b) shows the change in the intensity of the graphite peaks vs synthesis time.

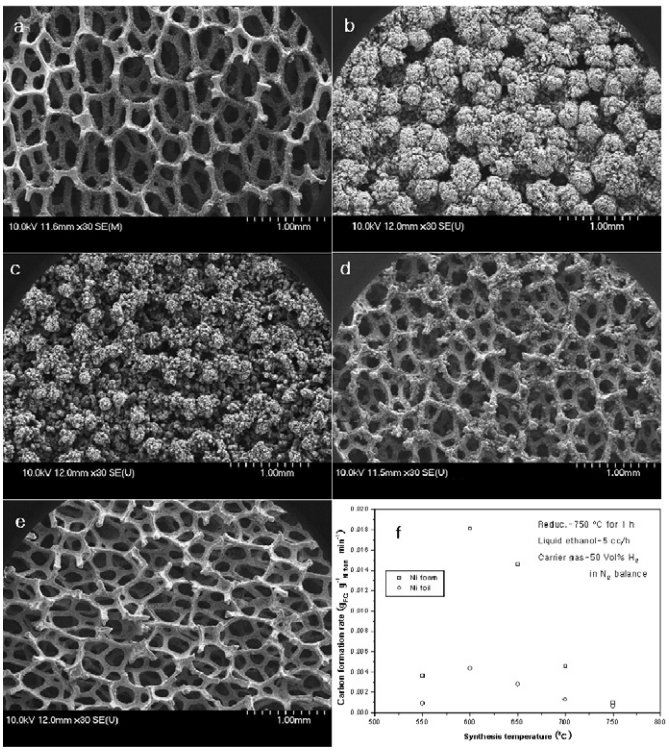

Fig. 4. SEM images of the filamentous carbon formed on the nickel foam with 50 vol% H_2 in N_2 at synthesis temperature of (a) 550, (b) 600, (c) 650, (d) 700, and (e) 750 °C. (f) shows the plot of carbon formation rate vs the synthesis temperature. Liquid ethanol was supplied at the rate of 5 cc/h. The nickel foams were reduced at 750 °C for 1 h in 50 vol% H_2 in N_2.

ethanol was supplied at a rate of 2 cc/h. The nickel foam was reduced at 700 °C for 1 h. The carrier gas of 30 vol% H_2 in N_2 was used for both reduction and growth processes. The formation rate increased slowly during the short exposure to ethanol vapor, and then increased rapidly until the synthesis time reached to 100 min, but slowed down thereafter. Fig. 3b shows the XRD patterns for the samples obtained with synthesis time of 10, 60, and 120 min. The nickel peaks were recorded at 2θ between 40° and 100°. The carbon peak appeared at approximately $2\theta = 26.5°$ after 60 min from the initiation of carbon formation. The position of the carbon peak agreed well with that of the representative graphite with an interlayer spacing corresponding to the (0 0 2) plane of bulk graphite, except that the peak appeared blunt compared with the bulk graphite peak. The intensity of the graphite peak represents the amount of carbon formed on the nickel foam. Thus, the variation in the intensity of the graphite peaks shown in Fig. 3b clearly indicates that the amount of carbon formed on the nickel foam increased as the synthesis time increased. These trends observed from Fig. 3 agrees well with those proposed in the previous study [16] that proved the initiation of CNF formation on the polycrystalline nickel by SEM and XRD approaches.

Figs. 4a–4e shows the SEM images of the filamentous carbon formed for 1 h using liquid ethanol supplied at a rate of 5 cc/h at various synthesis temperatures. The nickel foam was reduced at 750 °C for 1 h in 50 vol% H_2 in N_2. At 550 °C, the foam surface appeared to be covered with a thin layer of carbon. As the synthesis temperature increased to 600 °C, the amount of as-formed carbon increased tremendously. Micro-sized pores are barely visible over the nickel foam. At higher temperatures, however, carbon formation rate gradually declined, and at 750 °C the foam surface appeared clean. These results are summarized in Fig. 4f. A favorable temperature for a higher carbon formation should be in the range of 600–650 °C with the highest rate achieved around 600 °C. In addition, we compared the catalytic activity on nickel foam with that on nickel foil greater than 99.4% in purity. Cross section (10 mm × 10 mm: $W \times L$) and mass (approximately 50 mg) of nickel foil were similar to those of nickel foam. In the same synthesis conditions, trend of carbon formation rate with synthesis temperature was similar but more carbon was produced from Ni foam, in particular, around 600 °C. We can conclude that Ni foam is more useful for high productivity of filamentous carbon than Ni foil.

This trend can be explained by the catalytic pyrolysis of ethanol, which involves five sequential reactions proposed by Red'kin et al. [23]. They claimed that the presence of carbon dioxide in the reaction gas phase generated during the catalytic decomposition of ethanol on Ni catalysts validates the conclusive evidence of Boudouard reaction ($2CO = C + CO_2$). This means that among the five reactions, Boudouard reaction enables the key features of the synthesis of carbon nanomaterials from ethanol vapor: relatively low temperature and high selectivity of the process. Their proposal has been supported by other studies [24,25]. Although temperature with a maximum formation rate was a little lower, the results proposed by Red'kin et al. [23] seem to be in fair accordance with our results; the carbon formation rate reached a maximum at 600 °C and decreased sharply as the synthesis temperature increased (Fig. 4).

Fig. 5 shows a series of XRD patterns that correspond to the SEM images shown in Fig. 4. In Fig. 5a, five nickel metal diffraction peaks and a graphitic peak are evident at 2θ between 20° and 100°. Figs. 5a and 5c show that the intensity of the graphite peak detected at 2θ of about 26.5° varied according to the variation of synthesis temperature. The variation in the intensity of the graphite peak with synthesis temperature was consistent with the SEM images shown in Fig. 4. From the sharpness of the graphite peaks shown in Fig. 5c, however, it was difficult to determine whether as-foamed filamentous carbon was well-graphitized. We also identified seven peaks ($2\theta = 39.38°$, 41.72°, 58.62°, 71.40°, 78.29°, 86.11°, and 88.3°), as indicated at the bottom of Fig. 5b. These peaks can be attributed to the Ni_3C. The strongest Ni_3C peaks were observed at 550 °C, and the intensity of the Ni_3C peaks decreased as the synthesis temperature increased. Above 700 °C, the Ni_3C peaks nearly disappeared. Another Ni_3C peak was observed at 2θ of about 44.81° and indexed to the (1 1 3) plane. Fig. 5c shows that the Ni_3C peak of the (1 1 3) plane was strongest at 550 °C. Fig. 5d shows the variation of the nickel peaks detected at 2θ of about 92.95° and 98.48° at different synthesis temperatures. As the synthesis temperature decreased, not only was the peak shape gradually altered, but the sharpness and intensity were aggravated. This observation implies that the variation in the shape and intensity of the metallic nickel phase may be strongly related to the variation in both the activity and the crystalline size of the metallic nickel, which result from increased carbon deposition into the nickel metal and increased Ni_3C formation. These results are consistent with those of previous studies [26,27]. Another interesting result is that the Ni_3C peaks became weaker as the H_2 concentration in the carrier gas decreased to 30 vol% at 700 °C. Based on the results shown in Figs. 1 and 5, we can conclude that carbon rich conditions enhance the appearance of Ni_3C after longer exposure to ethanol.

In the carbon rich condition, metal nickel particles are easily carburized and deactivated during growth of filamentous carbon due to an increase in the carbon concentration in nickel. In this case, nickel carbide species may be present or generated in the nickel metal. However, these nickel carbide species are very unstable and easily decomposed into the graphite and metallic nickel at higher synthesis temperature—especially above 600 °C [28]. Therefore, these nickel carbide species are significantly different from the metastable Ni_3C [29]. Recently, it has been reported

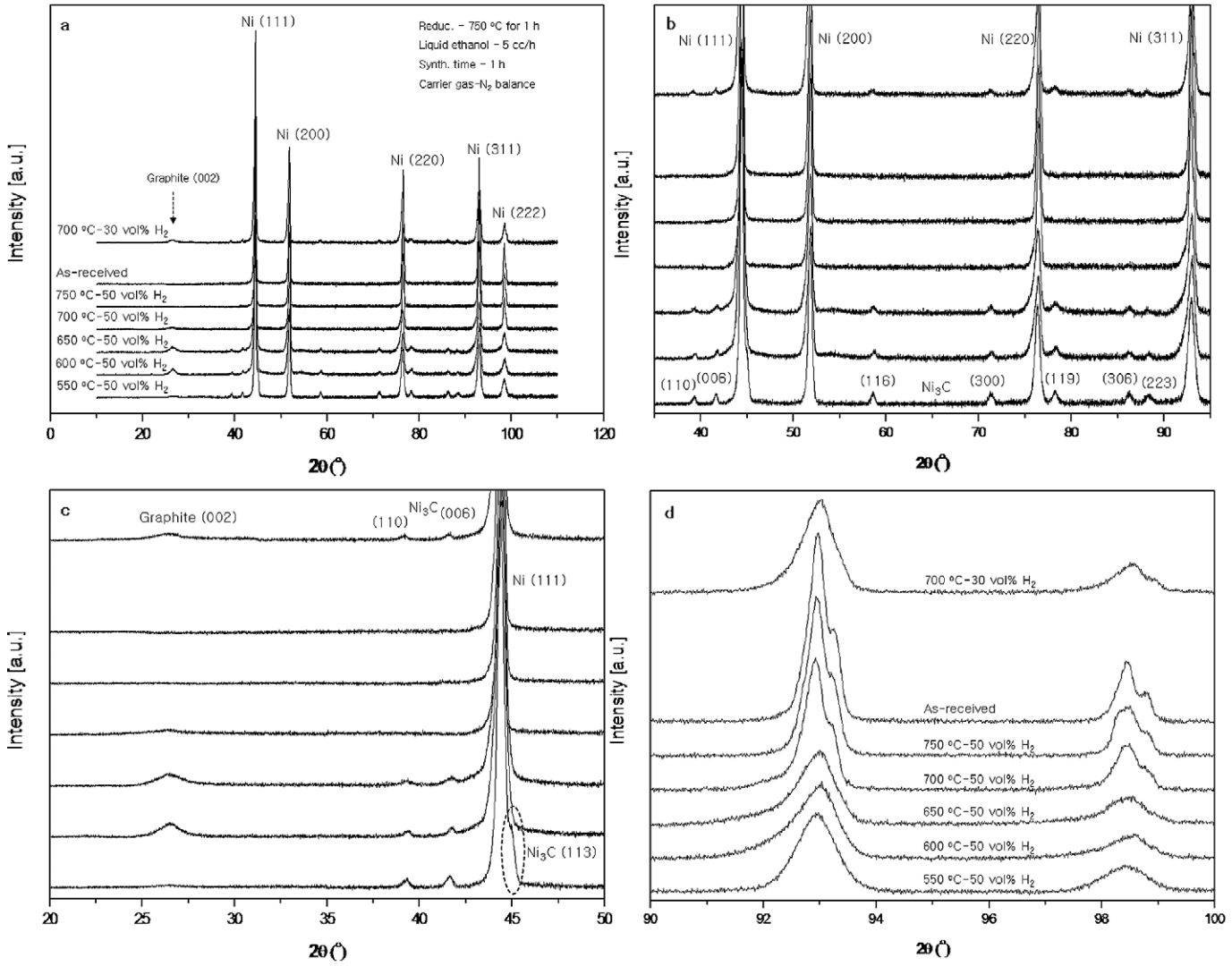

Fig. 5. XRD patterns corresponding to the SEM images in Fig. 4: (a) overview diffraction patterns, (b) Ni_3C patterns, (c) graphite patterns and (d) nickel patterns at 2θ of between 90° and 100°.

that during growth of filamentous carbon, metastable Ni_3C can be decomposed into the graphite and the metallic nickel under annealing conditions at temperature above 600 °C [30,31]. The Ni_3C can also be decomposed during the exposure to air even at room temperature due to the instability in air. Jarrah et al. discovered the existence of the Ni_3C that induced the initial growth of CNF through a relatively short exposure to air [16]. Ducati et al. identified the presence of Ni_3C at 550 and 700 °C. They suggested that the Ni_3C obtained at 700 °C might be formed after the growth process, upon cooling of Ni–C supersaturated interstitial solid solution due to rapid temperature decrease to less than 600 °C [32]. In contrast, at lower synthesis temperature, the nickel metal can undergo a favorable conversion to the metastable Ni_3C during growth [30,33]. Above studies, especially the model proposed by Ducati et al. [31], are useful for clarifying the formation mechanism of Ni_3C identified in this work, although Motojima et al. reported that Ni_3C was formed via decomposition of C_2H_2 on metallic nickel at 750 °C [34].

Fig. 6 shows the Raman spectroscopy of the samples synthesized at 550, 650, and 750 °C. The prepared nickel foam was reduced at 750 °C for 1 h. In the first-order Raman spectrum, the width of the peaks decreased as the synthesis temperature increased. At 550 °C, two peaks (D- and G-line) appeared broad and blunt, which is characteristic of amorphous or very disordered carbons. At 750 °C, however, the peaks were sharper and the G-line peak was much stronger than that of the D-line. Change in intensity ratio (I_D/I_G) is related to amorphization and graphitization of the sample [35]. Generally, the I_D/I_G ratio can be determined by the ratio of peak heights or peak areas [36]. When peak widths are not similar as shown in Fig. 6, the ratio of peak areas is more useful for evaluating the effect of material ordering. In this work, Lorentzian profiles were used as the simplest fits to calculate the ratio of peak areas. The I_D/I_G ratio was 2.7, 2.12, 0.66 for synthesis temperature of 550, 650, and 750 °C respectively. This trend is also observed for the second-order Raman spectrum, where the peaks were mostly measured at approximately 2460, 2707 (G'-line), 2947 (D + G-line), and 3251 cm^{-1} (2D'-line). At 750 °C, the strongest peak was observed at 2707 cm^{-1} (G'-line), indicative of a well-graphitized carbon structure. This result is similar to that observed in the multi-walled CNTs [37]. On the other hand, the G'-line peak became weaker and broader as synthesis temperature decreased, and an amorphous or a disordered carbon pattern was observed at 550 °C, as shown in the first-order Raman spectrum. Raman analysis indicates that the high synthesis temperature is responsible for the growth of well-graphitized filamentous carbon. Our results are consistent with previous study [38].

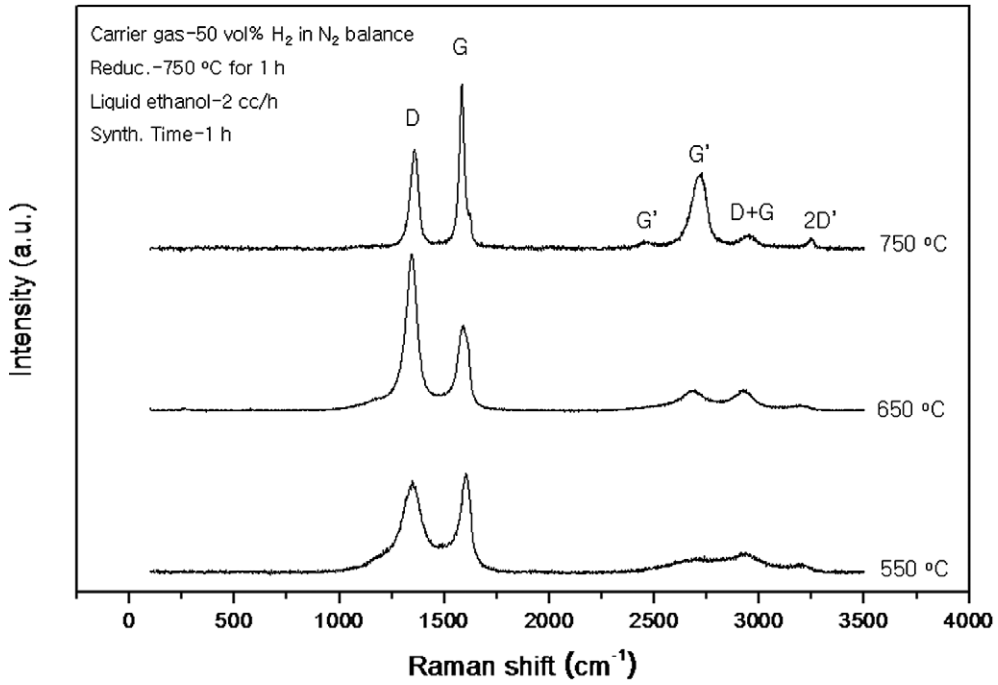

Fig. 6. Raman spectroscopy of as-formed filamentous carbons on the nickel foam with 50 vol% H_2 in N_2 at synthesis temperature of 550, 650, and 750 °C, respectively. Liquid ethanol was supplied at the rate of 5 cc/h. The nickel foams were reduced at 750 °C for 1 h in 50 vol% H_2 in N_2.

3.2. Morphology and growth mechanism of filamentous carbons: The role of catalytic particles and the effect of surface break-up

Fig. 7 shows the relationship between the filamentous carbon and the nickel nanoparticles formed on the foam surface in the absence of surface face break-up. The surface of as-received nickel foam before reduction is shown in Fig. 7a. The surface appeared clean and the grain size of the polycrystalline nickel foam was approximately 10 μm. The inset shows an EDX spectrum of Fig. 7a. Fig. 7b shows the surface morphology of the nickel foam after reduction for 1 h with 30 vol% H_2 in N_2. Many nanoparticles with diameters of 20–100 nm were uniformly distributed on the surface. Fig. 7c, an overview of the nickel foam after the growth process, shows the nanoparticles with diameters of 50–150 nm. The image reveals that the diameter of as-grown filaments is independent of nanoparticle size. The black arrow indicates the root of a filament where a nanoparticle was not clearly visible. Fig. 7d shows a filamentous carbon with a nanoparticle encapsulated at the tip. A large nickel particle with diameter of approximately 150 nm is marked with a white arrow in Fig. 7c. The particle has a quasi-spherical shape and was firmly attached to the surface of the nickel foam. Fig. 7e shows that the filamentous carbon with length of approximately 500 nm encapsulated nanoparticles at the tip. Fig. 7f shows an octopus-like carbon network grown on the surface of a quasi-spherical large nickel particle with a diameter of approximately 100 nm. Encapsulated nanoparticles were observed at the tip of the filaments. We suggest that the formation of the filamentous carbon on the surface of the nickel foam occurs primarily via the tip-growth mechanism, and that the diameter of filaments is not always dependent on the size of the nanoparticles where the growth initiates. A few studies of the octopus-like growth mechanism using nickel catalysts have been reported [39,40]. Pham-Huu et al. suggested that the octopus-like formation of CNFs is responsible for the tip-growth mechanism. This model agrees well with our proposed mechanism.

The samples in the TEM images of Fig. 8 were obtained at 650 °C (Figs. 8a and 8b) and 750 °C (Figs. 8c and 8d), respectively. Fig. 8a shows many wave-like carbon filaments. There were very narrow cavities or no cavity inside the filaments. The average outer diameter of the filaments was approximately 20 nm. Fig. 8b shows the tip of as-grown filamentous carbon, enclosing a nanoparticle approximately 15 nm in diameter, possibly of nickel. The outer

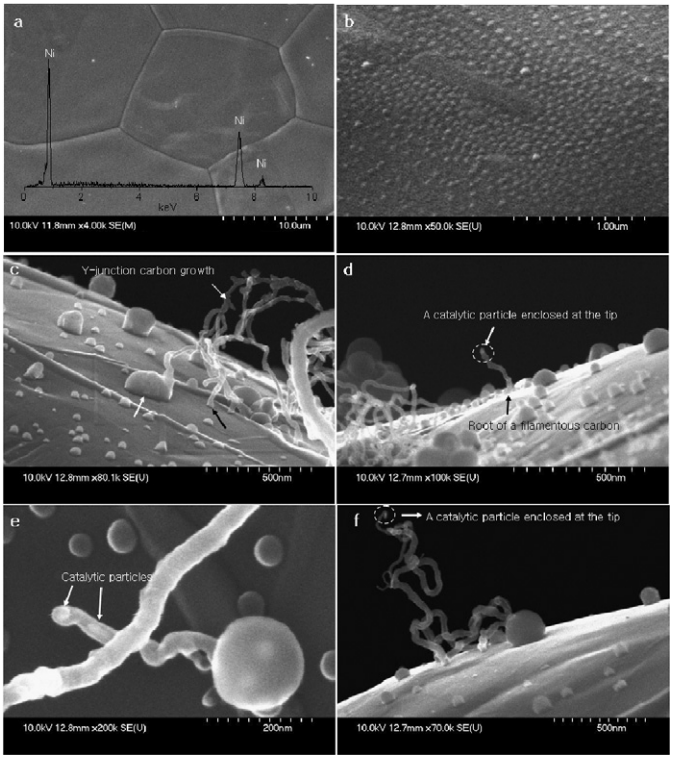

Fig. 7. Role of nickel nanoparticles in the growth of the filamentous carbon on the surface of the nickel foam. (a) SEM image and EDX graph of as-received nickel foam, (b) nickel nanoparticles formed on the nickel foam after reduction in 30 vol% H_2 in N_2, (c) overview of as-grown filamentous carbon, (d) size-dependent growth of a filamentous carbon from a small nickel nanoparticle (<50 nm), (e) size-independent growth of a filamentous carbon from a large nickel nanoparticle (>100 nm), and (f) octopus-like network formation of filamentous carbon.

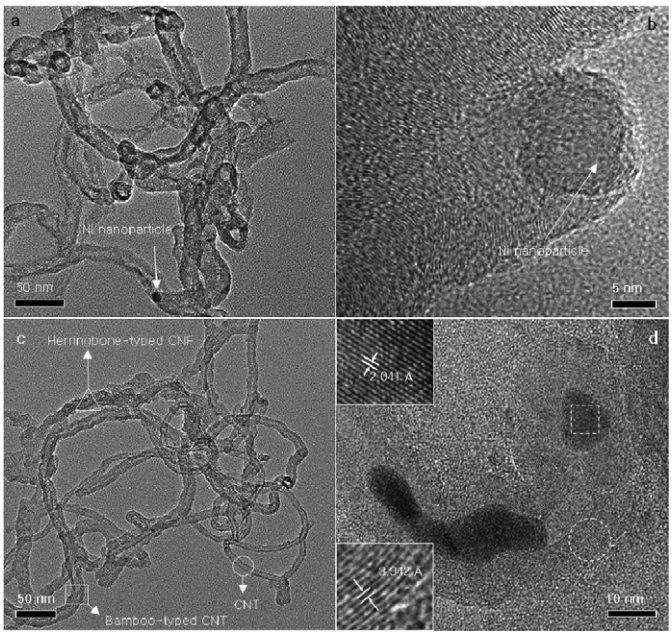

Fig. 8. TEM and HRTEM images obtained at 650 (a and b) and 750 °C (c and d): (a and c) as-grown filamentous carbons, (b) Tip of CNFs encapsulating a nickel nanoparticles and (d) tip of a CNT encapsulating two nickel nanoparticles. Upper and lower inserts in (d) show lattice spacings of a nickel nanoparticle in a high resolution image selected by the white square in (a) and graphitic shells shown in the high resolution image selected by the white circle in (a), respectively.

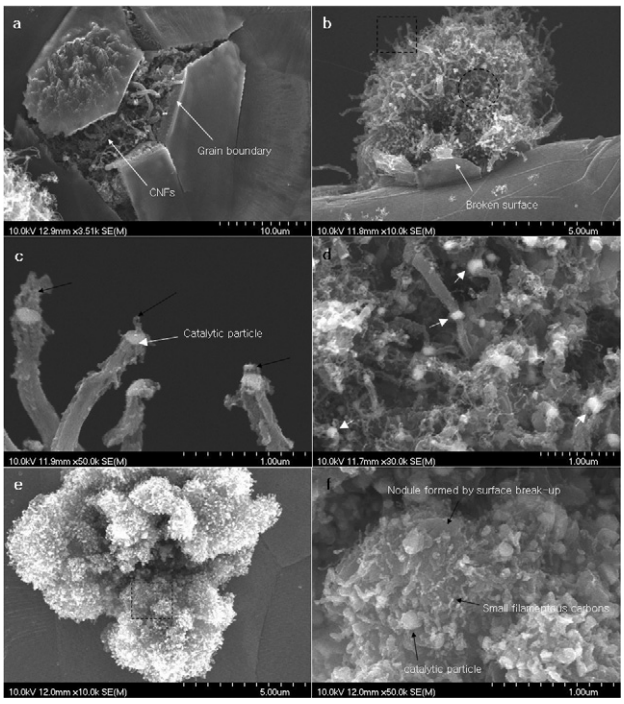

Fig. 9. SEM images of the surface break-up occurred on the surface of the nickel foam: (a) a partially cracked grain boundary, (b) a bunch of CNFs that was bloomed from the fragmentized surface, (c) the tip of CNFs encapsulating nanoparticles, (d) various CNFs formed during the surface break-up, (e) nodule-like structure that was formed as a result of surface break-up and (f) small carbon filaments and nanoparticles observed on the nodule-like structure.

shells of the filaments which were regarded as CNFs grown via the tip-growth mechanism were formed in a direction different from the growth direction of the filaments. Fig. 8c shows both the CNFs and the CNTs synthesized on the foam surface. Fig. 8d shows a filament with nanoparticles at its tip and stem. The particle remaining in the core appears elongated in the growth direction of the filament. The crystalline structure of the nanoparticle enclosed at the tip is shown in the upper inset (the area highlighted with the white square). The lattice spacing of 2.041 Å can be assigned to (1 1 1) lattice planes in metallic nickel. The lower inset (the area indicated by the white circle) displays the graphitic shells of the filamentous carbon with interspacing layers of approximately 3.342 Å, which is consistent with that of bulk graphite. These results agree well with those shown in Figs. 6 and 7.

In the presence of surface break-up, the shape and growth mechanism of filamentous carbon can be significantly altered. Fig. 9 shows the catalytic nanoparticles and the filamentous carbon that were formed during surface break-up. Fig. 9a shows the cracks generated along the grain boundary of the polycrystalline nickel foam. Very large and rough carbon filaments, considered as bulky CNFs, were observed at the gap. At this stage, the grain boundary did not appear completely fragmented. Fig. 9b shows a bunch of CNFs. At the bottom of the blooming carbon flower, it is clearly shown that the foam surface was broken and opened fully. Fig. 9c, a high-resolution image of Fig. 9b (black square), shows the catalytic nanoparticle enclosed at the tip of the CNF with a diameter of approximately 150 nm. Fig. 9c also shows another CNF that was branched off on a facet of the nanoparticle (black arrows). Fig. 9d shows the inner part of the bunch (black circle of Fig. 9d) where CNFs of various shapes and sizes were shown, in particular, multi-CNFs grown on a nanoparticle. Fortunately, we found a special bunch with an incomplete CNF formation. Fig. 9e shows the nanoparticles and the filamentous carbons formed during surface break-up. The bunch appeared to be composed of some large nodules that were projected from the broken surface. The protrusions were irregularly shaped, similar to popcorn. In addition, some filamentous carbon was formed on the protrusions. Fig. 9f shows a high resolution image of Fig. 9e (black square). The detail shown in the image reveals that the small filaments less than 30 nm in diameter were formed on the surface of the large nodule, but their yield was very low. We also found non-uniform, large nanoparticles on the nodules, which were similar in size to those shown in Fig. 9d (20–200 nm). These nanoparticles did not appear to induce the formation of filamentous carbon. Unlike the nanoparticles observed on the surface of the nickel foam in Fig. 7, the nanoparticles in Fig. 9 have very various forms and sizes.

According to the above observation, we propose the bunch growth mechanism of filamentous carbon via surface break-up as follows. It is generally known that metal surfaces can be fragmentized by metal dusting corrosion which is caused by precipitation of a secondary phase due to high carbon accumulation into the metal surface, resulting in the formation of metal carbides and filamentous carbons on the surface [41,42]. In the present work, Fig. 9 well explains the surface break-up mechanism that results from this corrosion phenomenon. During an early stage of the surface break-up, nanoparticles may be formed on or with nodules generated by explosion of the foam surface. These nanoparticles are the impure nickel metal rather than the metastable Ni_3C. Nickel carbide species might be present or carbon atoms might have been dissolved in the nickel metal due to bulk diffusion of the carbon released by the catalytic decomposition of ethanol prior to surface break-up. Once the surface is cracked, carbon deposition into the broken surface accelerates this process, and the various carbon filaments are initiated on the nanoparticles. During or after growth process, the nickel nanoparticles can be converted into the metastable Ni_3C by varying both the synthesis temperature and carbon concentration in the furnace. Figs. 10 and 11 provide evidence of our proposed mechanism.

Fig. 10 shows the TEM images of CNFs obtained at 550 °C using 30 (a and b) and 50 vol% H_2 (c and d) in N_2. Fig. 10a, an

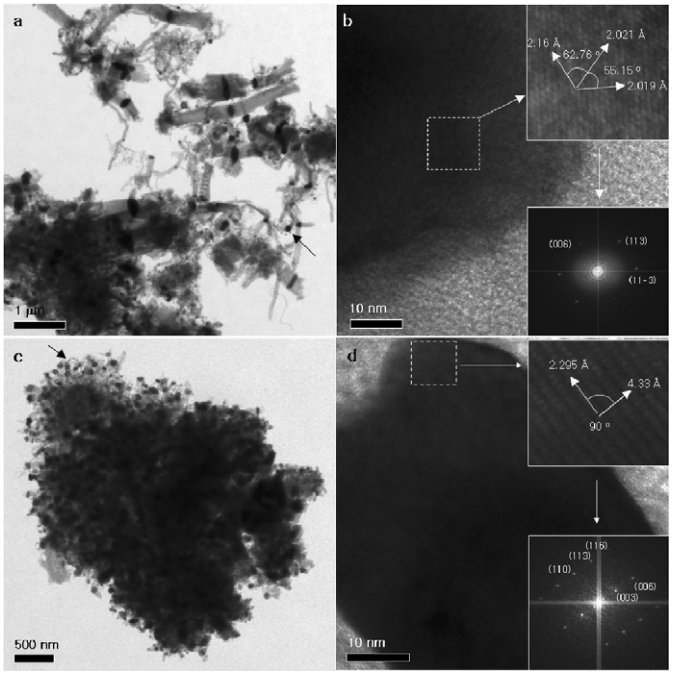

Fig. 10. TEM and DDP images of as-formed product at 550 °C in 30 (a and b) and 50 (c and d) vol% H_2 in N_2. The particles were identified as Ni_3C (rhomberhedral).

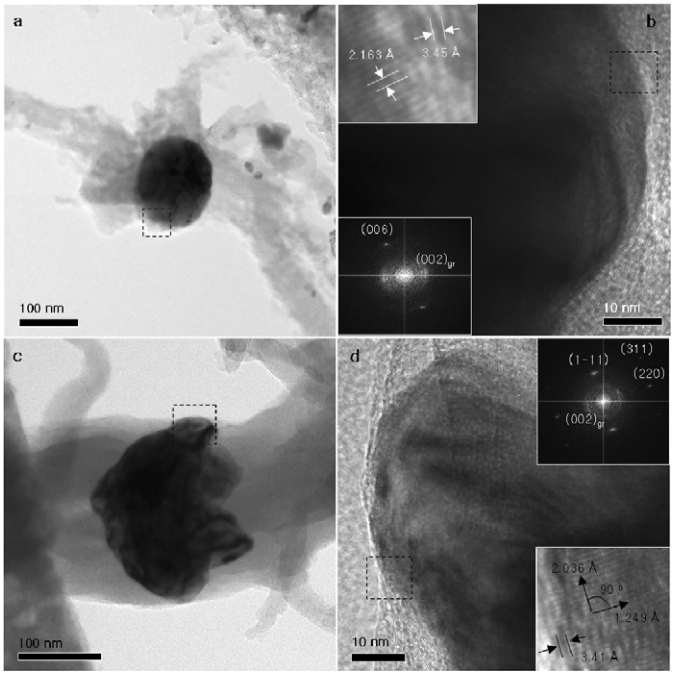

Fig. 11. TEM and DDP images of as-formed product at 700 °C in 30 (a and b) and 50 (c and d) vol% H_2 in N_2. The particles in (b) and (d) were identified as Ni_3C (rhombohedral) and nickel metal (cubic), respectively.

overview of the sample, reveals that various CNFs are formed and their shapes were highly consistent with those shown in the presence of surface break-up (SEM image of Fig. 9d). Fig. 10b shows the high resolution TEM (HRTEM) images and digital diffraction pattern (DDP) of a nanoparticle (circle in Fig. 10a). The 2.019, 2.021, and 2.16 Å lattice spacings were calculated from the DDP, and the angles among the lattices are approximately 62.76 and 55.12°. These lattice spacings can be assigned to the (1 1 3), (1 1 −3), and (0 0 6) lattice planes in Ni_3C (rhombohedral), respectively. Fig. 10c shows the TEM image of the sample in the SEM image of Fig. 9f. CNFs were short and very irregular in shape. Fig. 10d is a high resolution image of the nanoparticle selected in Fig. 10c. The calculated lattice spacings were approximately 2.295, 2.021, 1.569, 2.159, and 4.318 Å. DDP and HRTEM results reveal that the calculated lattice planes correspond to the (1 1 0), (1 1 3), (1 1 6), (0 0 6), and (0 0 3) planes identified in Ni_3C. In particular, Fig. 10 shows the presence of the (1 1 3) lattice plane which was detected in the XRD pattern of the sample obtained at 550 °C (as shown in Fig. 5c). It is clear from these observations that the formation of Ni_3C occurs dominantly at 550 °C.

Fig. 11 shows the TEM images of CNFs obtained at 700 °C with 30 (a and b) and 50 vol% (c and d) H_2 in N_2. Fig. 11a shows the bulky CNFs grown on a large nanoparticle with a diameter of approximately 150 nm. From the HRTEM image and the DDP of Fig. 11a (Fig. 11b), the lattice spacing was estimated to be 2.163 Å. This plane was consistent with the (0 0 6) plane of Ni_3C. In addition, a lattice plane corresponding to the (0 0 2) plane of bulk graphite was observed in the HRTEM image (lattice spacing of approximately 3.45 Å). Fig. 11c shows a nanoparticle that induced two different CNFs. From DDP analysis of the HRTEM image (upper inset of Fig. 11d), we identified that the large nanoparticle was metallic nickel (cubic). Lattice spacings corresponding to the (1 −1 1), (2 2 0), and (3 1 1) planes of Ni_3C were calculated to be 2.036, 1.249, and 1.065 Å respectively. The results of Figs. 10 and 11 were consistent with the XRD patterns shown in Fig. 5.

The growth mechanism of as-grown filamentous carbon in this study can be developed from the models proposed by Sacco et al. [43] and Jablonski et al. [44], which explained the growth mechanism of filamentous carbon on α-Fe and Fe, Co, and Ni foils, respectively. In particular, Jablonski et al. emphasized that extensive and continued surface break-up increases the weight gain rate. They also claimed that, unlike Fe and Co, surface break-up phenomenon did not occur on Ni foil at 623 °C. However, in our experiments, surface break-up occurred on the nickel foam at 623 °C. We also found that surface break-up can be induced by tuning the synthesis temperature and other synthesis conditions, such as the amount of liquid ethanol supplied into the furnace, and, in particular, the concentration of H_2 in the carrier gas.

Based on our experiments using the nickel foam, we suggest a growth model illustrated in Fig. 12. In the first step (a), the carbons released from the decomposition of ethanol are deposited on the surface of both the nickel nanoparticles (C_{SS}) and polycrystalline nickel foam (C_{FS}). Then, the deposited carbon diffuses into the bulk nickel (C_{NS} and C_{FB}). The surface of the foam can be partially or completely covered with a thin carbon layer (C_{FS}), and carbide is formed on the surface of the nickel nanoparticles. Bulk diffusion into the nanoparticles ($C_{NS} \rightarrow C_{NB}$) occurs as carbon concentration at the interface of surface carbide and metal nanoparticle (C_{NS}) increases gradually. Then, the nanoparticle induces the formation of filamentous carbon (b). As-formed filaments are mainly responsible for the tip-growth mechanism. Higher concentrations of H_2 in the carrier gas would facilitate the removal of both the surface carbon and the chemisorbed species, resulting in the accumulation of the surface carbon layer. Consequently the formation of bulk carbide in the nickel foam can be limited, and surface break-up is inhibited. In this case, growth of the filamentous carbon on the nickel nanoparticles formed on the foam surface can be only completed by steps (a) and (b). This understanding can be clearly confirmed by the results shown in Fig. 7. On the other hand, the continuous increase of the bulk diffusion into the nickel foam, which results from accumulation of the deposited carbon, facilitates the formation of the carbide in polycrystalline nickel and enlarges the stress zone (c). In particular, the stress increases significantly at the grain boundary, initiating partial fragmenting of the boundary. Once a gap is generated at the grain boundary, carbon rapidly accumulates into the gaps. During this stage, some CNFs are observed at

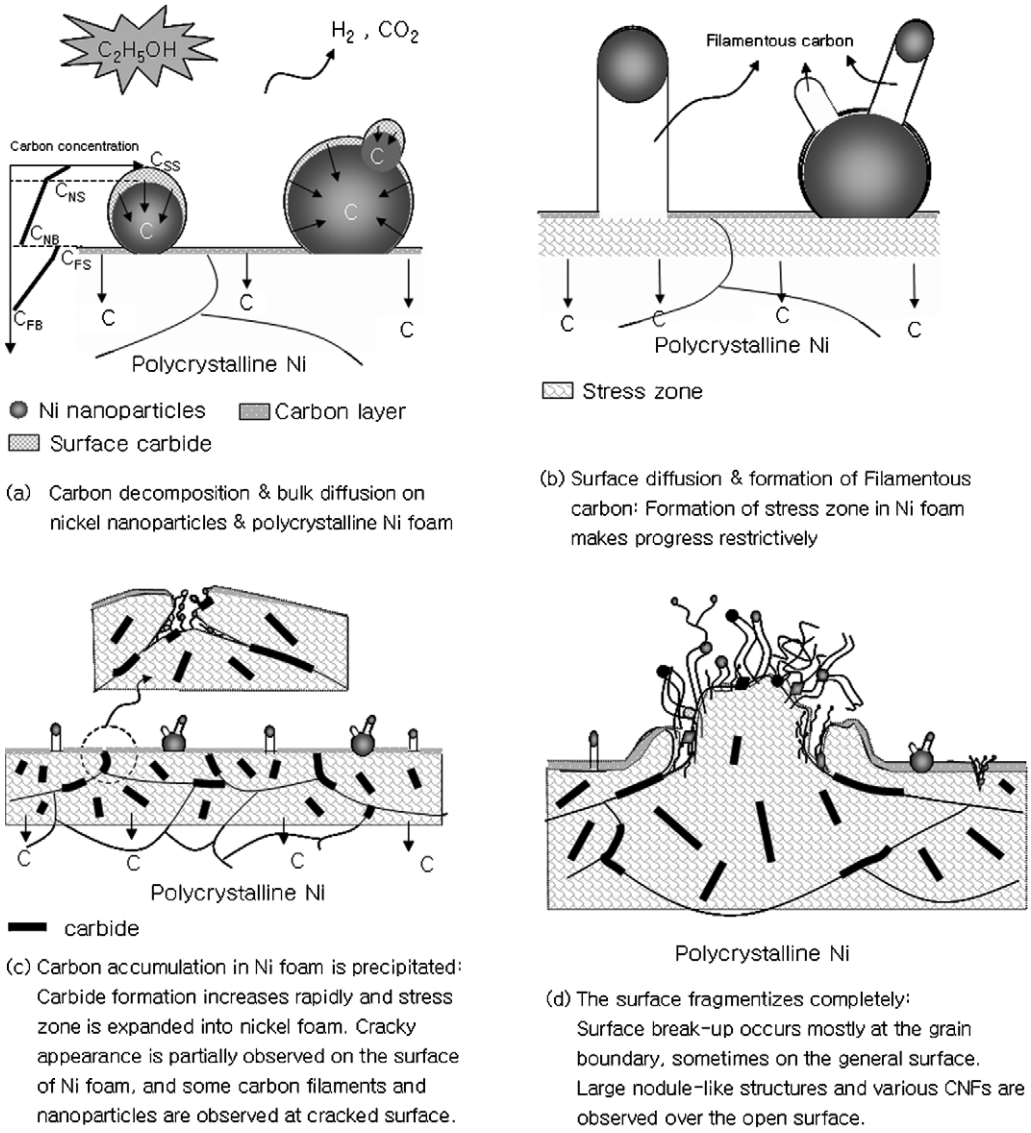

Fig. 12. Mechanism for the carbon formation on the nickel foam.

the cracked surface (as shown in Fig. 9a). Subsequently, the surface of the polycrystalline nickel foam opens fully as the amount of deposited carbon increases successively (surface break-up) (d). Nodule-like structures and many nickel nanoparticles project from the open surface. Finally, various CNFs sprout from these nanoparticles and the bunch of CNFs is completed.

4. Conclusion

This paper describes the growth of nano-sized filamentous carbon by catalytic decomposition of ethanol on polycrystalline nickel foam. The effects of synthesis conditions on carbon formation were investigated in detail. The formation rate of filamentous carbon decreased at higher H_2 concentration in the carrier gas and with less liquid ethanol supplied during the growth process. The carbon formation rate increased with longer synthesis time but gradually slowed down after 100 min. The study of synthesis temperature revealed that a favorable temperature for the maximum carbon formation rate was around 600 °C. Based on the XRD patterns, it was discovered that Ni_3C could be formed under some synthesis conditions (low synthesis temperature and carbon rich conditions) after a long exposure to ethanol vapor. It was demonstrated in detail that the surface morphology of the nickel foam has an important influence on the growth mechanism of filamentous carbons. Without the surface break-up, the nickel nanoparticles formed on the surface of the nickel foam acted as catalytic sites where the filamentous carbons started to grow. These nanoparticles were mostly observed at the tip of the filaments. Most filaments were CNFs, and CNTs were formed at higher synthesis temperatures. The diameters of the carbon filaments was approximately 20–30 nm. Nanoparticles less than 50 nm in diameter led to the formation of filamentous carbon of the same size. The octopus-like network with multiple small filaments was mainly observed from particles greater than 100 nm in diameter. In contrast, the surface break-up that occurred at the grain boundary led to a rapid increase in the carbon formation rate on the polycrystalline nickel foam. Various nickel nanoparticles and CNFs were observed at the fragmented surface. The TEM and DDP analyses supported the presence of the Ni_3C peaks recorded in the XRD pattern. In conclusion, we believe that the presence of surface break-up increases the carbon formation rate on the nickel foam, although the quality of as-grown carbon filaments requires further investigation.

Acknowledgments

The authors thank Chong-hyu Kim and Kwang-sik Myung (the Korea Institute of Energy Research: KIER) for their assistance (supplying the nickel foam and performing the SEM analysis). We also thank Yun-chang Park (the National Nano Fab Center: NNFC) for performing the TEM analysis. This work was supported by the KIER and the Korea Research Foundation Grant (KRF-J03000).

References

[1] S. Iijima, Nature 354 (1991) 56.
[2] R.H. Baughman, A.A. Zakhidov, W.A. de Heer, Science 297 (2002) 787.
[3] V.P. Veedu, A. Cao, X. Li, K. Ma, C. Soldano, S. Kar, P.A. Ajayan, M.N. Ghasemi-nezhad, Nat. Mater. 5 (2006) 457.
[4] D. Chen, K.O. Christensen, E.O. Fernandez, Z. Yu, B. Totdal, N. Latorre, A. Monzon, A. Holmen, J. Catal. 229 (2005) 82.
[5] C. Park, M.A. Keane, J. Catal. 221 (2004) 386.
[6] S. Noda, H. Sugime, T. Osawa, Y. Tsuji, S. Chiashi, Y. Murakami, S. Maruyama, Carbon 44 (2006) 1414.
[7] P.K. De Bokx, A.J.H.M. Kock, E. Boellaard, W. Klop, J.W. Geus, J. Catal. 96 (1985) 454.
[8] Y. Murakami, Y. Miyauchi, S. Chiashi, S. Maruyama, Chem. Phys. Lett. 377 (2003) 49.
[9] S. Park, D. Lee, Carbon 44 (2006) 1930.
[10] F. Xu, X. Liu, S.D. Tse, Carbon 44 (2006) 570.
[11] R.T.K. Baker, M.A. Barber, P.S. Harris, F.S. Featers, R.J. Waite, J. Catal. 26 (1972) 51.
[12] Z. Fan, J. Chen, K. Cui, F. Sun, Y. Xu, Y. Kuang, Electrochim. Acta 52 (2007) 2959.
[13] W. Wunderlich, Diamond Relat. Mater. 16 (2007) 369.
[14] E.F. Kukovitsky, S.G. L'vov, N.A. Sainov, V.A. Shustov, Appl. Surf. Sci. 215 (2003) 201.
[15] N.A. Jarrah, F. Li, J.G.V. Ommen, L. Lefferts, J. Mater. Chem. 15 (2005) 1946.
[16] N.A. Jarrah, J.G.V. Ommen, L. Lefferts, J. Catal. 239 (2006) 460.
[17] M. Cantoro, V.B. Golovko, F. Hofmann, D.R. Williams, C. Ducati, J. Geng, B.O. Boskovic, B. Kleinsorge, D.A. Jefferson, A.C. Ferrari, B.F.G. Johnson, J. Robertson, Diamond Relat. Mater. 14 (2005) 733.
[18] N. Jeong, Y. Seo, J. Lee, Diamond Relat. Mater. 16 (2007) 600.
[19] C. Pham-huu, R. Vieira, B. Louis, A. Carvalho, J. Amadou, T. Dintzer, M.J. Ledoux, J. Catal. 240 (2006) 194.
[20] G.A. Jablonski, F.W.A.H. Geurts, A. Sacco, R.R. Biederman, Carbon 30 (1992) 87.
[21] T. Baird, J.R. Fryer, B. Grant, Carbon 12 (1974) 591.
[22] Y. Nishiyama, Y. Tamai, J. Catal. 45 (1976) 1.
[23] A.N. Red'kin, V.A. Kipin, L.V. Malyarevich, Inorg. Mater. 42 (2006) 242.
[24] P. Chen, H.B. Zhang, G.D. Lin, Q. Hong, K.R. Tsai, Carbon 35 (1997) 1495.
[25] A.G. Nasibulin, A. Moisala, D.P. Brown, E.I. Hauppinen, Carbon 41 (2003) 2711.
[26] O.S. Morozova, G.N. Kryukova, A.V. Ziborov, L.M. Plyasova, J. Catal. 144 (1993) 50.
[27] Y. Li, B. Zhang, X. Xie, J. Liu, Y. Xu, W. Shen, J. Catal. 238 (2006) 412.
[28] V.B. Avdeeva, O.V. Goncharova, D.I. Kochubey, V.I. Zaikovskii, L.M. Plyasova, B.M. Novgorodov, Sh.K. Shaikhutdinov, Appl. Catal. A 141 (1996) 117.
[29] S. Takenaka, H. Ogihara, K. Otsuka, J. Catal. 238 (2006) 412;
S. Takenaka, H. Ogihara, K. Otsuka, J. Catal. 208 (2002) 54.
[30] H. Nakano, J. Nakamura, Surf. Sci. 482–485 (2001) 341.
[31] S.R. Nishitani, K.N. Ishihara, R.O. Suzuki, P.H. Shingu, J. Mater. Sci. Lett. 4 (1985) 872.
[32] C. Ducati, I. Alexandrou, M. Chhowalla, J. Robertson, G.A.J. Amaratunga, J. Appl. Phys. 95 (2004) 6387.
[33] H. Nakano, J. Ogawa, J. Nakamura, Surf. Sci. 514 (2002) 256.
[34] S. Motojima, S. Asakura, M. Hirata, H. Iwanaka, Mater. Sci. Eng. B 34 (1995) L9.
[35] S. Urbonaite, L. Hälldahl, G. Svensson, Carbon 46 (2008) 1942.
[36] A.C. Ferrai, J. Robertson, Phys. Rev. B 61 (2000) 14095.
[37] M.S. Dresselhaus, G. Dresselhaus, R. Saito, A. Jorio, Phys. Rep. 409 (2005) 47.
[38] Y. Lee, N. Kim, J. Park, J. Han, Y. Choi, H. Ryu, H. Lee, Chem. Phys. Lett. 372 (2003) 853.
[39] T.M. Tavares, C.A. Bernardo, I. Alstrup, J.R. Rostrup-Nielsen, J. Catal. 100 (1986) 545.
[40] C. Pham-Huu, R. Vieira, B. Louis, A. Carvalho, J. Amadou, T. Dintzer, M.J. Ledoux, J. Catal. 240 (2006) 194.
[41] B. Schmid, N. Aas, Ø. Grong, R. Ødegård, Appl. Catal. 215 (2001) 257.
[42] P.E. Nolan, D.C. Lynch, A.H. Cutler, Carbon 32 (1994) 477.
[43] A. Sacco, P. Thacker, T.N. Chang, A.T.S. Ching, J. Catal. 85 (1984) 224.
[44] G.A. Jablonski, F.W.A.H. Geurts, A. Sacco, Carbon 30 (1992) 99.